From negative to positive magnetoresistance in the intrinsic magnetic topological insulator $MnBi_2Te_4$

Peng-Fei Zhu,[1] Xing-Guo Ye,[1] Jing-Zhi Fang,[2] Peng-Zhan Xiang,[1] Rong-Rong Li,[1] Dai-Yao Xu,[3] Zhongming Wei,[2] Jia-Wei Mei,[4] Song Liu,[4] Da-Peng Yu,[4] and Zhi-Min Liao[1,5,6,*]

[1]*State Key Laboratory for Mesoscopic Physics and Frontiers Science Center for Nano-optoelectronics, School of Physics, Peking University, Beijing 100871, China*

[2]*State Key Laboratory of Superlattices and Microstructures, Institute of Semiconductors, Chinese Academy of Sciences & Center of Materials Science and Optoelectronics Engineering, University of Chinese Academy of Sciences, Beijing 100083, People's Republic of China*

[3]*School of Science, Beijing Jiaotong University, Beijing, 100044, China*

[4]*Shenzhen Institute for Quantum Science and Engineering and Department of Physics, Southern University of Science and Technology, Shenzhen 518055, China*

[5]*Beijing Key Laboratory of Quantum Devices, Peking University, Beijing 100871, China*

[6]*Collaborative Innovation Center of Quantum Matter, Peking University, Beijing 100871, China*

(Received 10 December 2019; accepted 7 February 2020; published 24 February 2020)

We report the magnetotransport properties of $MnBi_2Te_4$ thin flakes through gate modulation at low temperatures. Under in-plane magnetic field, a large negative magnetoresistance (MR) maintains up to 10 T, which is related to the suppression of spin scattering when the magnetic order is gradually forced into the ferromagnetic (FM) state. Under perpendicular magnetic field, a steep resistance decrease is observed around ∼3 T, corresponding to the transition from an antiferromagnetic (AFM) to a canted AFM (CAFM) state. Due to the net Berry curvature, a notable anomalous Hall effect is observed and can be effectively tuned by gate voltages. The enhanced Hall coefficient would emerge under high magnetic fields when the Fermi level is close to the charge neutral point. Moreover, a transition from negative to positive MR is obtained when increasing the magnetic field. A large linear positive MR occurs around ∼8 T, corresponding to the CAFM-FM transition. The nonsaturated positive MR here may have a similar mechanism to the one in Weyl semimetals, revealing the strong combination between topology and magnetism in $MnBi_2Te_4$.

DOI: 10.1103/PhysRevB.101.075425

I. INTRODUCTION

The combination between topology and magnetism has attracted increasing interest recently [1–4], especially since the quantum anomalous Hall (QAH) effect was proposed to be hosted by magnetic topological insulator (TI) [5], and experimentally realized in Cr-doped $(Bi, Sb)_2Te_3$ [6,7]. The QAH effect can only be observed at extreme low temperatures in such magnetically doped TIs with complex chemical compositions [6,7]. Recently, an intrinsic magnetic TI, $MnBi_2Te_4$, was proposed to host various tunable topological quantum states [8–16], including the QAH insulators, which can be observed even at high temperature ∼60 K [17].

$MnBi_2Te_4$ is van der Waals layered ternary tetradymite compound with the space group $R\bar{3}m$, which consists of stacking septuple layers (SLs) along the c axis [18,19]. The layered surface is usually denoted as ab plane. Each SL can be viewed as a Bi_2Te_3 quintuple layer intercalated with a Mn-Te bilayer in the center. The magnetic moment is mainly provided by Mn^{2+} ion by $\sim 5\,\mu_B$ per Mn^{2+} (μ_B is the Bohr magneton) [9]. Below the Néel temperature $T_N \sim 25$ K [8,20], each SL forms a ferromagnetic (FM) order ground state with an out-of-plane easy axis due to the intralayer exchange coupling [8,9,19]. Intriguingly, neighboring SLs demonstrate antiferromagnetic (AFM) order caused by the interlayer coupling [8,9]. Therefore, bulk $MnBi_2Te_4$ is an A-type AFM TI [8]. The cleavage surface of $MnBi_2Te_4$ is inherently gapped due to the intralayer FM order on the surface [21], which is a necessary condition to realize the QAH states [9] or the long-sought axion insulator states [22,23]. Thus, $MnBi_2Te_4$ provides an ideal platform to investigate exotic physical phenomena, including the QAH effect, topological magnetoelectric effects, and topological superconductivity [8]. Importantly, in contrast with theoretical predication that $MnBi_2Te_4$ is inherently gapped on the cleavage surface, the high-resolution angle-resolved photoemission spectroscopy (ARPES) shows gapless topological surface states [24–28]. Such a gapless Dirac cone is very robust against temperature or surface perturbation [26]. The discrepancy between theory and ARPES results may be caused by the surface structural deformation or spin reorientation on the surface [26,28]. For now, this question remains debatable.

Recently, the QAH state and the axion insulator at zero field have been observed in exfoliated $MnBi_2Te_4$ films with odd [29] and even [30] layers, respectively. Also, high-Chern-number QAH ($C = 2$) has been obtained in the nine SLs $MnBi_2Te_4$ nanodevices [17]. Moreover, $MnBi_2Te_4$ is also proposed to host a Weyl semimetal (WSM) phase [9,10]. When the magnetic order of $MnBi_2Te_4$ is tuned from the AFM

*liaozm@pku.edu.cn

state to the FM state by applying an external magnetic field parallel to the c axis (i.e., the spin-easy axis), type-II WSM phase with a single pair of Weyl nodes usually can emerge [10,12]. When the magnetic orientation is rotated away from the c axis, a transition from a type-II WSM to a type-I WSM phase can occur at a specific angle [10]. When further rotating the magnetic orientation perpendicular to the c axis, the Weyl nodes overlap with each other and induce a phase transition to a trivial insulator [10,31].

Despite the clean limit samples, which theory predictions consider only up to now [8–15], the $MnBi_2Te_4$ samples with moderate disorders and vacancies also need to be carefully investigated for future application. It has been reported that antisite defects and Mn vacancies are contained in the bulk $MnBi_2Te_4$ samples [20]. Strong spin fluctuation in this system may induce large surface gap ($\sim$85 meV) even in the paramagnetic (PM) state [21]. All these results indicate that $MnBi_2Te_4$ samples with moderate disorders and vacancies may have distinct physical properties from the clean limit samples.

In this work, the magnetotransport properties of more than 20 $MnBi_2Te_4$ thin flakes with thickness around $10 \sim 20$ nm were measured through back gate modulation at low temperatures. The results are highly repeatable and three typical devices are presented in the main text. Magnetoresistance (MR) was measured for both $\mathbf{H} \parallel ab$ plane (in-plane magnetic field) and $\mathbf{H} \parallel c$ axis (perpendicular magnetic field). For $\mathbf{H} \parallel c$ axis, two clear inflection points of MR with increasing magnetic field indicate the AFM-canted AFM (CAFM) transition and CAFM-FM transition, respectively. In addition, a notable anomalous Hall effect (AHE) was observed within the CAFM regime, which is attributed to the net Berry curvature. Importantly, a transition from negative to positive MR was observed by rotating the magnetic field from $\mathbf{H} \parallel ab$ plane to $\mathbf{H} \parallel c$ axis, which may be related to the possible formation of the WSM phase within the FM order, revealing the strong combination between topology and magnetism in $MnBi_2Te_4$. Besides, an enhanced Hall coefficient under high magnetic fields was found when the Fermi level is close to the charge neutral point.

II. METHOD

The $MnBi_2Te_4$ thin flakes were first obtained by mechanical exfoliation and then transferred onto substrates. The electrodes were prepared by standard electron beam lithography. The atomic resolution high angle annular dark field scanning transmission electron microscope (HAADF-STEM) images [Figs. 1(a) and 1(b)] of the cross section of a typical exfoliated $MnBi_2Te_4$ thin flake clearly show the SL layered structural of $MnBi_2Te_4$, indicating the single crystal samples. Figure 1(c) shows the scanning electron microscope (SEM) image of a typical $MnBi_2Te_4$ sample. The thickness of a typical $MnBi_2Te_4$ thin flake measured by an atomic force microscope is shown in Fig. 1(d) around $\sim$12.7 nm.

III. RESULTS AND DISCUSSION

The magnetotransport properties of device S1 with thickness $\sim$15.1 nm are shown in Fig. 2. The temperature dependence of longitudinal resistance R_{xx} shows an apparent inflection point around the Néel temperature $T_N \sim 25$ K [Fig. 2(a)] [21,32–34]. Above T_N, R_{xx} decreases with decreasing temperature, showing a metallic behavior. A metal-insulator transition occurs below T_N, which may be related to the formation of AFM order [8]. The formation of the AFM order can induce gap opening on the surface [8], which would drive the system into the insulating region. The magnetic field dependence of R_{xx} for both $\mathbf{H} \parallel ab$ plane and $\mathbf{H} \parallel c$ axis under different temperatures are shown in Figs. 2(b) and 2(c), respectively. For $\mathbf{H} \parallel ab$ plane, the resistance decreases gradually with increasing magnetic fields, which shows the AFM state is gradually transformed into the FM state. Further, the interlayer AFM order can give rise to strong spin scattering, which can cause high resistivity [20,21,35]. However, such spin scattering can be suppressed when the system is forced into FM phase by applying external magnetic fields [20,21]. Thus, R_{xx} decreases with increasing fields. In addition, after the complete FM order, the negative MR reaches saturation with the magnitude of $\sim -22\%$ at 1.6 K above $\sim$10.5 T. The critical magnetic field decreases with increasing temperature, which is consistent with pervious observations [20]. Considerable negative MR can also be obtained for temperature above T_N as shown in Fig. 2(b), indicating that strong spin scattering still exists even for the paramagnetic order [21] with MR $\sim -5\%$ under $\mu_0 H = 14$ T at 25 K.

For $\mathbf{H} \parallel c$ axis, a significant decrease can be found around $\mu_0 H \sim 3$ T [denoted by the red arrow in Fig. 2(c)], which is attributed to the transition from AFM state to CAFM state driven by the out-of-plane magnetic field. The CAFM state is a metastable state with noncollinear spin structure before the system is fully polarized to FM order [20,21] [see the inset of Fig. 3(c) for the schematic diagram of AFM, CAFM, and FM order, respectively], which has been confirmed by neutron scattering measurements [21]. The steep decrease here indicates spin scattering is strongly suppressed in the CAFM state. The MR increases again within the CAFM order, which may be attributed to the positive MR background induced by orbit effect [36]. Intriguingly, the steep decrease disappears for temperature above T_N as shown in Fig. 2(c), which is consistent with the scenario of spin scattering strongly suppressed by CAFM order. To distinguish from the $\mathbf{H} \parallel c$ situation, the steep decrease does not show up for the $\mathbf{H} \parallel ab$ plane, indicating the absence of the metastable CAFM state in the $\mathbf{H} \parallel ab$ plane case, which is consistent with the out-of-plane easy axis in $MnBi_2Te_4$ [8,9].

Another inflection point can be found around $\mu_0 H \sim 8$ T for $\mathbf{H} \parallel c$ [denoted by the blue arrow in Fig. 2(c)], which is attributed to the transition from CAFM order to FM order (see the analysis of S2 below). The MR shows a large nonsaturated linear behavior after the complete FM order, which is similar to the scenario of the WSMs [36–38], like the TaAs family [39]. It is worth noting that the WSM phase indeed can emerge in $MnBi_2Te_4$ within the FM order [10]. Thus, the nonsaturated linear MR here may have similar mechanism to the one of WSMs. While for the $\mathbf{H} \parallel ab$ plane, the MR shows weak dependence under high magnetic fields, which is consistent with the theoretical prediction that a phase transition from WSM to trivial insulator [10].

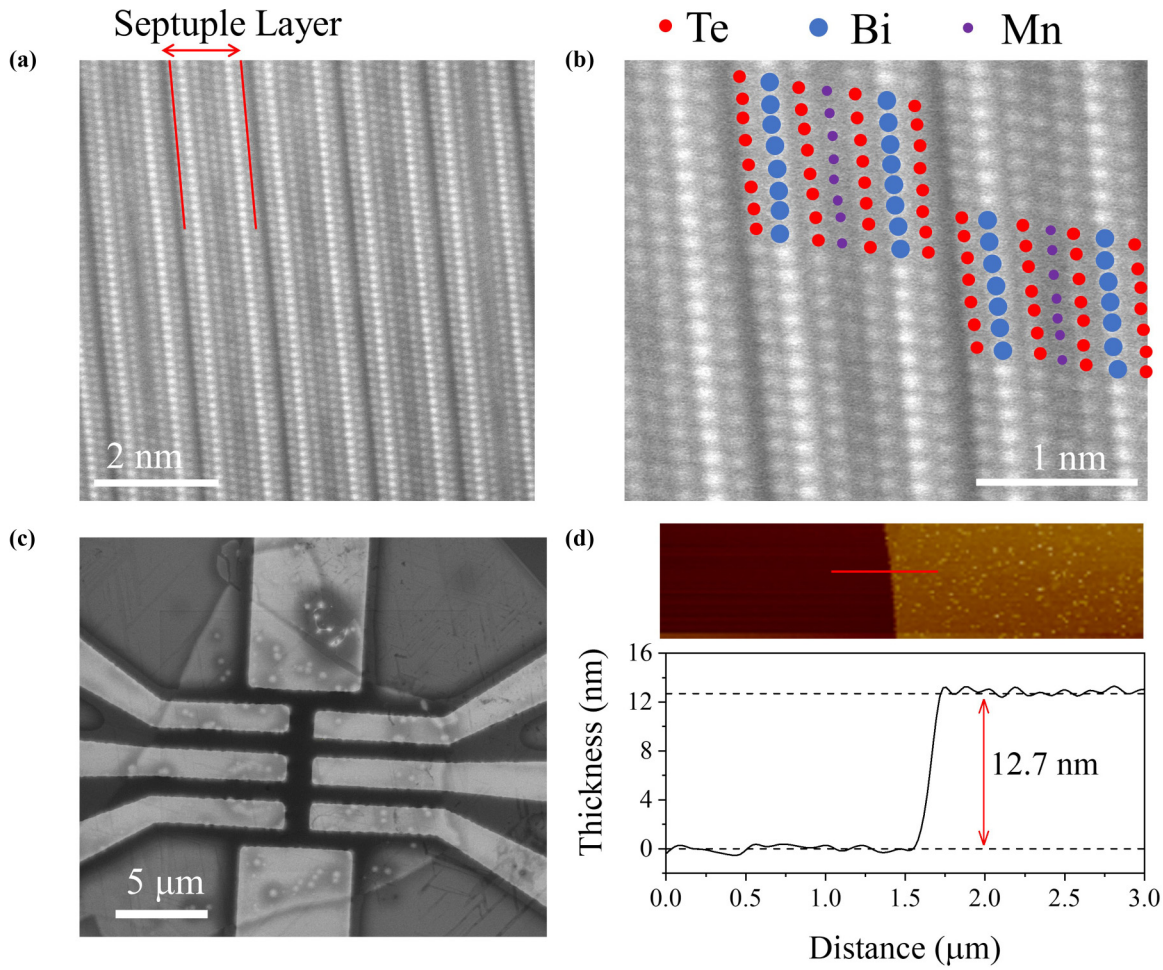

FIG. 1. Characterizations of $MnBi_2Te_4$ thin flakes. (a) The HAADF-STEM image of the cross section of a typical exfoliated $MnBi_2Te_4$ thin flake. (b) Zoom-in view of the HAADF-STEM image shown in (a), on which the layered $MnBi_2Te_4$ structural model is overlaid. (c) SEM image of a typical $MnBi_2Te_4$ device. (d) The atomic force microscope image and the line profile along the red line of a typical $MnBi_2Te_4$ thin flake.

Figure 3 shows the Hall resistivity R_{xy} of device S2 with thickness ∼13.9 nm under different gate voltages at 1.6 K. The transfer curve [Fig. 3(a)] indicates device S2 is dominated by hole-type carriers at $V_g = 0$ V. Significant AHE can be found within the CAFM regime, as shown in Fig. 3(b). When magnetic field is above ∼8 T, ordinary linear Hall effect emerges due to the single-band nature of this system. The carrier density estimated through Hall coefficient is ∼5.8 × 10^{19} cm^{-3} at $V_g = 0$ V.

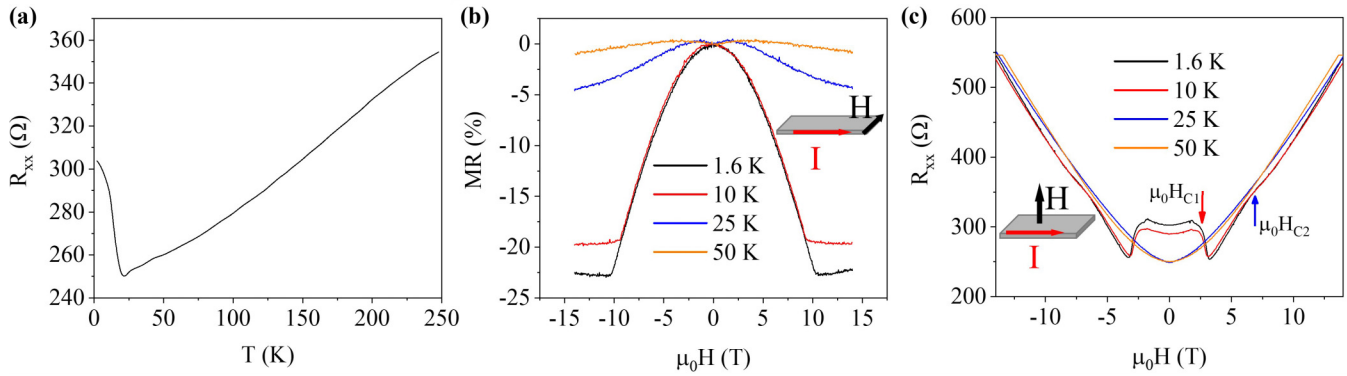

FIG. 2. Temperature dependence of magnetotransport for device S1. (a) Temperature-dependence of R_{xx} with antiferromagnetic transition around ∼25 K. The magnetoresistance at different temperatures for (b) **H** ∥ *ab* plane and (c) **H** ∥ *c* (the easy axis). The insets of (b) and (c) illustrate the magnetic field orientation.

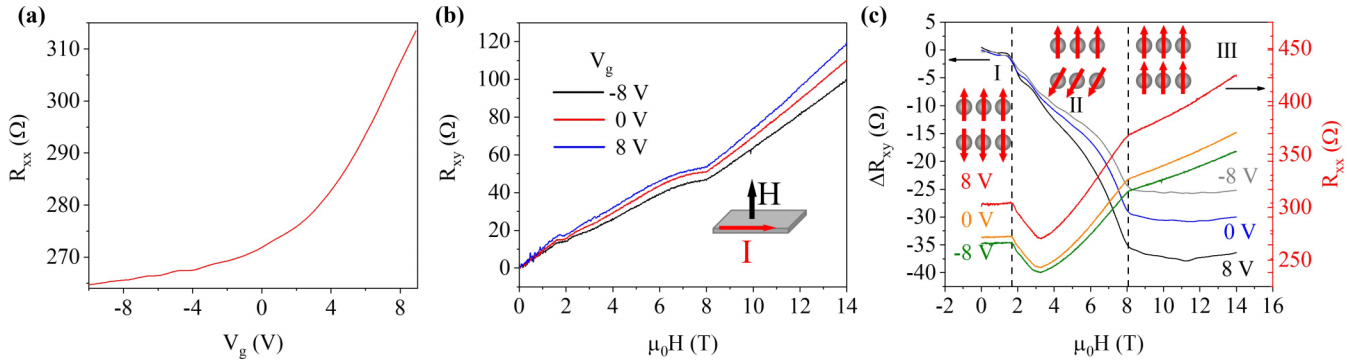

FIG. 3. Hall resistance with gate modulation for device S2. (a) The R_{xx} as a function of gate voltages at 1.6 K. (b) Hall resistance at 1.6 K under different gate voltages. The inset illustrates the relative orientation of the magnetic field. (c) Anomalous Hall resistance ΔR_{xy} and R_{xx} versus out-of-plane magnetic fields at 1.6 K under different gate voltages. ΔR_{xy} is obtained by subtracting the linear background under high fields. The inset shows the schematic diagram of I: AFM, II: CAFM and III: FM order, respectively.

To get a better observation of AHE in the CAFM regime, the linear background (i.e., the ordinary Hall effect) is subtracted, and notable AHE $\Delta R_{xy}(H)$ is shown in Fig. 3(c). Importantly, the AHE becomes more significant when the Fermi level is close to the charge neutral point. The enhanced AHE with tuning the Fermi level close to the charge neutral point indicates the AHE origin from the intrinsic net Berry curvature [40–43], which is induced by the noncollinear spin structure [21]. The magnetic-field dependence of R_{xx} is also plotted in Fig. 3(c). The inflection points in $\Delta R_{xy}(H)$ and $R_{xx}(H)$ are well matched, which ensures that the inflection points of R_{xx} indeed originates from the transition from AFM to CAFM order and CAFM to FM order, respectively. In addition, the nonsaturated linear dependence of R_{xx} can also be found within the FM phase for device S2, which is similar to that of device S1. It is worth noting that the inflection points $\mu_0 H_{C1}$ and $\mu_0 H_{C2}$ are independent of the back gate [Fig. 3(c)], indicating the intrinsic magnetic origin of the inflection points.

Another device S3 with thickness ∼12.5 nm, which has reachable charge neutral point, was investigated to further reveal the exotic physical properties of $MnBi_2Te_4$. Figure 4(a) shows the gate dependence of R_{xx} at 1.6 and 25 K, respectively. At 1.6 K, the charge neutral point with maximum resistance occurs around $V_g \sim -78$ V. With increasing temperature to 25 K, the charge neutral point shows a shift to the negative gate voltage, which can be explained by the increasing electron density by thermal activation [44]. Fig. 4(b) shows the temperature-dependence of R_{xx} under different gate voltages. Under $V_g = 0$ V, the resistance decreases with decreasing temperature above T_N, indicating a metallic behavior. However, by tuning the Fermi level close to the charge neutral point, the metallic behavior transforms into insulator-like behavior, which indicates the Fermi level is tuned into the bulk gap. The MR measured at 1.6 K shows similar behaviors when the gate voltage is tuned far away from the charge neutral point [Fig. 4(c)]. However, different from devices S1 and S2, the AFM-CAFM transition for device S3 has two inflection points near the charge neutral point [denoted by the green arrows in Fig. 4(c)]. Near the charge neutral point, moderate disorders may lead to a small thermal activation gap, thus both electrons and holes could contribute to the transport measurements. The two inflection points here should be attributed to the critical points of the suppression of spin scattering for electrons and holes, respectively, indicating the asymmetrical transport of electrons and holes in $MnBi_2Te_4$.

The Hall measurements at 1.6 K are shown in Fig. 4(d) and the carrier density ∼2.2 $\times 10^{19}$ cm^{-3} at $V_g = 0$ V is estimated. Similar to device S2, the AHE is enhanced when the Fermi level is close to the charge neutral point. Near the charge neutral point (such as $V_g = -95$ V), the Hall resistance is nearly zero and shows weak-fieldresponse under low magnetic fields, while a positive Hall coefficient emerges under high magnetic fields. Within the AFM phase, the cleavage surface is gapped due to the intralayer FM order on the surface [9]. As the Fermi level is tuned into the gap, both electrons and holes participate in the transport due to the thermal activation. The two-carrier compensation would lead to the nearly zero Hall coefficient. However, when the system is forced into the FM phase under high magnetic fields, the gap would be closed due to the possible formation of the WSM phase [10]. The Fermi level is located at a fixed band within the FM regime since the gap is closed. Thus, the compensation between electrons and holes is suppressed and only one carrier dominates the transport. In addition, the emergent Berry curvature within the WSM phase could also contribute to the Hall coefficient. Thus, a positive Hall coefficient would emerge within the FM order. However, it is worth noting that the significant differences of Hall coefficient between the two states may only be partially explained by the above reasons. The intrinsic mechanism of such intriguing phenomenon should be further investigated.

Through our experimental efforts, it is worth noting that $MnBi_2Te_4$ samples with moderate disorders and with thickness between the two-dimensional (2D)-limit ultrathin films and 3D bulks may possess distinct physical properties, in contrast to $MnBi_2Te_4$ thin films less than 9 SLs [17,29,30] or bulk samples [20,21]. The linear MR behavior is quite different from the bulk samples reported previously. The absence of signatures of QAHE may be attributed to the quantum confinement induced small gap hindered by thermal activation and moderated disorders. However, the WSM phase may possibly emerge in this condition, thus the transport

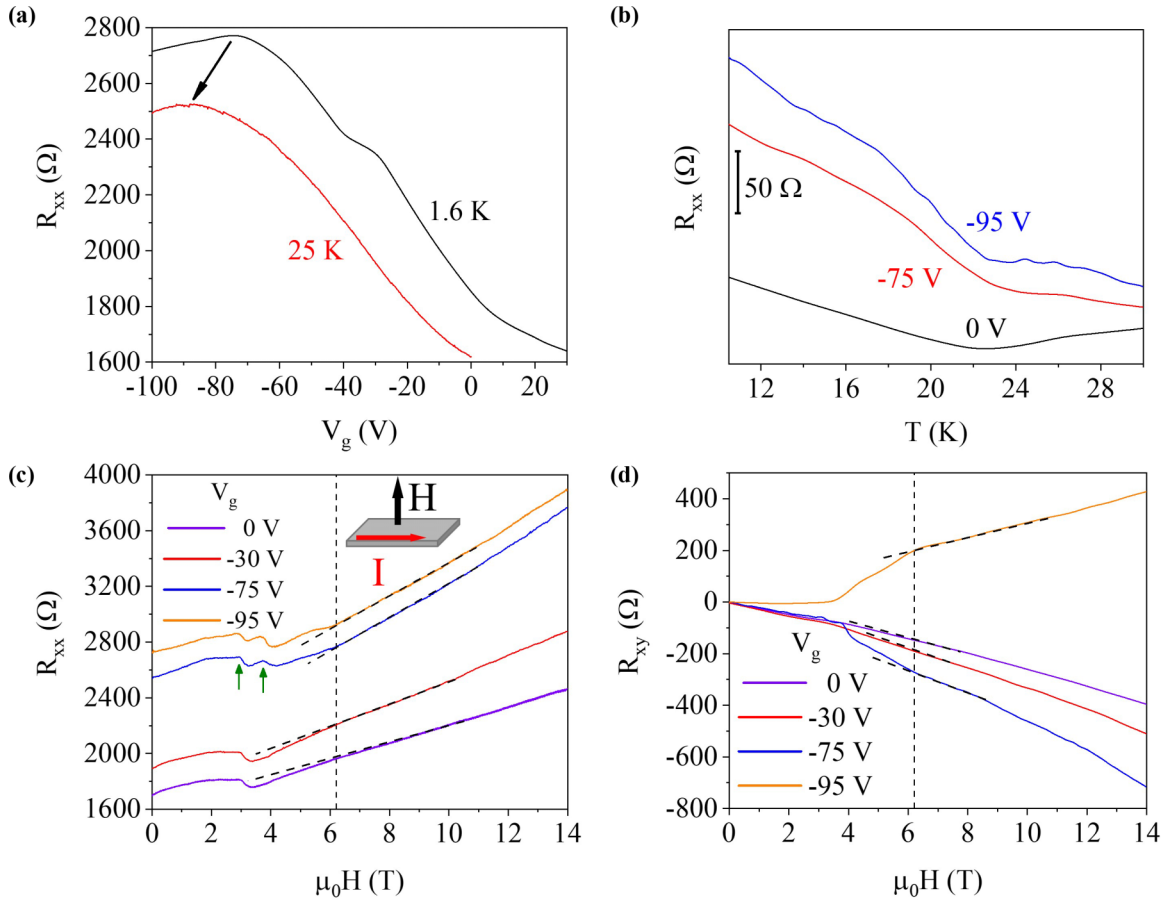

FIG. 4. Magnetotransport with observable charge neutral point for device S3. (a) Gate dependence of R_{xx} at 1.6 and 25 K. The charge neutral point with maximum R_{xx} emerges around ~ -78 V at 1.6 K. (b) R_{xx} versus temperature under different gate voltages. (c) R_{xx} as a function of magnetic field under different gate voltages at 1.6 K. The inset illustrates the out-of-plane magnetic field. (d) Hall resistance as a function of magnetic fields under different gate voltages at 1.6 K. The dashed lines are used to indicate the CAFM-FM transition clearer.

signatures such as chiral anomaly may be further discovered in such $MnBi_2Te_4$ systems.

IV. CONCLUSION

In summary, through the detailed magnetotransport measurements of $MnBi_2Te_4$ thin flakes, the AFM-CAFM-FM transition for **H** ∥ *c* axis and the AFM-FM transition for **H** ∥ *ab* plane are clearly observed, indicating that $MnBi_2Te_4$ is an A-type AFM material with out-of-plane easy axis. A notable AHE can be significantly tuned by gate voltage, which is attributed to the net Berry curvature. When the Fermi level is close to the charge neutral point, an enhanced Hall coefficient under high magnetic fields is observed. In addition, a metal-insulator transition occurs through gate modulation, while the magnetic properties are almost unchanged with varying gate voltages. Negative MR is observed when the field is applied in the *ab* plane, which is related to the gradual AFM-FM transition. Nevertheless, a large linear MR is obtained within the FM order for **H** ∥ *c* axis. Such a transition is consistent with the theory prediction that a transition from trivial insulator to WSM when rotating the magnetic field from **H** ∥ *ab* plane to **H** ∥ *c* axis, indicating the strong combination between magnetism and topological electronic structure in $MnBi_2Te_4$.

ACKNOWLEDGMENTS

This work was supported by National Key Research and Development Program of China (No. 2018YFA0703703 and No. 2016YFA0300802), and National Natural Science Foundation of China (No. 91964201, No. 61825401, and No. 11774004).

[1] F. D. M. Haldane, Phys. Rev. Lett. **61**, 2015 (1988).
[2] M. Z. Hasan and C. L. Kane, Rev. Mod. Phys. **82**, 3045 (2010).
[3] X.-L. Qi and S.-C. Zhang, Rev. Mod. Phys. **83**, 1057 (2011).
[4] Y. Tokura, K. Yasuda, and A. Tsukazaki, Nat. Rev. Phys. **1**, 126 (2019).
[5] R. Yu, W. Zhang, H.-J. Zhang, S.-C. Zhang, X. Dai, and Z. Fang, Science **329**, 61 (2010).
[6] C.-Z. Chang, J. Zhang, X. Feng, J. Shen, Z. Zhang, M. Guo, K. Li, Y. Ou, P. Wei, L.-L. Wang *et al.*, Science **340**, 167 (2013).

[7] C.-Z. Chang, W. Zhao, D. Y. Kim, H. Zhang, B. A. Assaf, D. Heiman, S.-C. Zhang, C. Liu, M. H. W. Chan, and J. S. Moodera, Nat. Mater. **14**, 473 (2015).

[8] M. M. Otrokov, I. I. Klimovskikh, H. Bentmann, A. Zeugner, Z. S. Aliev, S. Gass, A. U. B. Wolter, A. V. Koroleva, D. Estyunin, A. M. Shikin *et al.*, Nature (London) **576**, 416 (2019).

[9] J. Li, Y. Li, S. Du, Z. Wang, B.-L. Gu, S.-C. Zhang, K. He, W. Duan, and Y. Xu, Sci. Adv. **5**, eaaw5685 (2019).

[10] J. Li, C. Wang, Z. Zhang, B.-L. Gu, W. Duan, and Y. Xu, Phys. Rev. B **100**, 121103(R) (2019).

[11] M. M. Otrokov, I. P. Rusinov, M. Blanco-Rey, M. Hoffmann, A. Y. Vyazovskaya, S. V. Eremeev, A. Ernst, P. M. Echenique, A. Arnau, and E. V. Chulkov, Phys. Rev. Lett. **122**, 107202 (2019).

[12] D. Zhang, M. Shi, T. Zhu, D. Xing, H. Zhang, and J. Wang, Phys. Rev. Lett. **122**, 206401 (2019).

[13] Y. Peng and Y. Xu, Phys. Rev. B **99**, 195431 (2019).

[14] B. Chen, F. Fei, D. Zhang, B. Zhang, W. Liu, S. Zhang, P. Wang, B. Wei, Y. Zhang, Z. Zuo *et al.*, Nat. Commun. **10**, 4469 (2019).

[15] M. Z. Shi, B. Lei, C. S. Zhu, D. H. Ma, J. H. Cui, Z. L. Sun, J. J. Ying, and X. H. Chen, Phys. Rev. B **100**, 155144 (2019).

[16] J. Zhang, Z. Liu, and J. Wang, Phys. Rev. B **100**, 165117 (2019).

[17] J. Ge, Y. Liu, J. Li, H. Li, T. Luo, Y. Wu, Y. Xu, and J. Wang, arXiv:1907.09947.

[18] D. S. Lee, T.-H. Kim, C.-H. Park, C.-Y. Chung, Y. S. Lim, W.-S. Seo, and H.-H. Park, Crystallogr. Eng. Commun. **15**, 5532 (2013).

[19] A. Zeugner, F. Nietschke, A. U. B. Wolter, S. Gaß, R. C. Vidal, T. R. F. Peixoto, D. Pohl, C. Damm, A. Lubk, R. Hentrich *et al.*, Chem. Mater. **31**, 2795 (2019).

[20] J. Cui, M. Shi, H. Wang, F. Yu, T. Wu, X. Luo, J. Ying, and X. Chen, Phys. Rev. B **99**, 155125 (2019).

[21] S. H. Lee, Y. Zhu, Y. Wang, L. Miao, T. Pillsbury, H. Yi, S. Kempinger, J. Hu, C. A. Heikes, P. Quarterman *et al.*, Phys. Rev. Research **1**, 012011(R) (2019).

[22] X.-L. Qi, T. L. Hughes, and S.-C. Zhang, Phys. Rev. B **78**, 195424 (2008).

[23] J. Wang, B. Lian, X.-L. Qi, and S.-C. Zhang, Phys. Rev. B **92**, 081107(R) (2015).

[24] Y. J. Chen, L. X. Xu, J. H. Li, Y. W. Li, H. Y. Wang, C. F. Zhang, H. Li, Y. Wu, A. J. Liang, C. Chen *et al.*, Phys. Rev. X **9**, 041040 (2019).

[25] Y. Gong, J. Guo, J. Li, K. Zhu, M. Liao, X. Liu, Q. Zhang, L. Gu, L. Tang, X. Feng *et al.*, Chin. Phys. Lett. **36**, 076801 (2019).

[26] Y.-J. Hao, P. Liu, Y. Feng, X.-M. Ma, E. F. Schwier, M. Arita, S. Kumar, C. Hu, R. Lu, M. Zeng *et al.*, Phys. Rev. X **9**, 041038 (2019).

[27] H. Li, S.-Y. Gao, S.-F. Duan, Y.-F. Xu, K.-J. Zhu, S.-J. Tian, J.-C. Gao, W.-H. Fan, Z.-C. Rao, J.-R. Huang, J.-J. Li *et al.*, Phys. Rev. X **9**, 041039 (2019).

[28] P. Swatek, Y. Wu, L.-L. Wang, K. Lee, B. Schrunk, J. Yan, and A. Kaminski, arXiv:1907.09596.

[29] Y. Deng, Y. Yu, M. Z. Shi, Z. Guo, Z. Xu, J. Wang, X. H. Chen, and Y. Zhang, Science, **367**, 895 (2020).

[30] C. Liu, Y. Wang, H. Li, Y. Wu, Y. Li, J. Li, K. He, Y. Xu, J. Zhang, and Y. Wang, Nat. Mater. (2020), doi: 10.1038/s41563-019-0573-3.

[31] Z. Wang, H. Weng, Q. Wu, X. Dai, and Z. Fang, Phys. Rev. B **88**, 125427 (2013).

[32] J. G. Checkelsky, M. Lee, E. Morosan, R. J. Cava, and N. P. Ong, Phys. Rev. B **77**, 014433 (2008).

[33] T. J. Liu, X. Ke, B. Qian, J. Hu, D. Fobes, E. K. Vehstedt, H. Pham, J. H. Yang, M. H. Fang, L. Spinu *et al.*, Phys. Rev. B **80**, 174509 (2009).

[34] S. Yang, Z. Li, C. Lin, C. Yi, Y. Shi, D. Culcer, and Y. Li, Phys. Rev. Lett. **123**, 096601 (2019).

[35] M. Zhu, T. Hong, J. Peng, T. Zou, Z. Q. Mao, and X. Ke, J. Phys.: Condens. Matter **30**, 075802 (2018).

[36] T. Liang, Q. Gibson, M. N. Ali, M. Liu, R. J. Cava, and N. P. Ong, Nat. Mater. **14**, 280 (2015).

[37] H. Weng, C. Fang, Z. Fang, B. Andrei Bernevig, and X. Dai, Phys. Rev. X **5**, 011029 (2015).

[38] A. Narayanan, M. D. Watson, S. F. Blake, N. Bruyant, L. Drigo, Y. L. Chen, D. Prabhakaran, B. Yan, C. Felser *et al.*, Phys. Rev. Lett. **114**, 117201 (2015).

[39] S. M. Huang, S. Y. Xu, I. Belopolski, C. C. Lee, G. Chang, B. Wang, N. Alidoust, G. Bian, M. Neupane, C. Zhang *et al.*, Nat. Commun. **6**, 7373 (2015).

[40] N. Nagaosa, J. Sinova, S. Onoda, A. H. MacDonald, and N. P. Ong, Rev. Mod. Phys. **82**, 1539 (2010).

[41] D. Xiao, M.-C. Chang, and Q. Niu, Rev. Mod. Phys. **82**, 1959 (2010).

[42] J. G. Checkelsky, R. Yoshimi, A. Tsukazaki, K. S. Takahashi, Y. Kozuka, J. Falson, M. Kawasaki, and Y. Tokura, Nat. Phys. **10**, 731 (2014).

[43] S. Nakatsuji, N. Kiyohara, and T. Higo, Nature (London) **527**, 212 (2015).

[44] C.-Z. Li, J.-G. Li, L.-X. Wang, L. Zhang, J.-M. Zhang, D. Yu, and Z.-M. Liao, ACS Nano **10**, 6020 (2016).